Pushing the boundaries of chemistry?
It takes #HumanChemistry

Make your curiosity and talent as a chemist matter to the world with a specialty chemicals leader. Together, we combine cutting-edge science with engineering expertise to create solutions that answer real-world problems. Find out how our approach to technology creates more opportunities for growth, and see what chemistry can do for you at:

evonik.com/career

ADVANCED FUNCTIONAL MATERIALS
www.afm-journal.de

Phase Selection in Mn–Si Alloys by Fast Solid-State Reaction with Enhanced Skyrmion Stability

Zichao Li, Yufang Xie, Ye Yuan,* Yanda Ji, Viktor Begeza, Lei Cao, René Hübner, Lars Rebohle, Manfred Helm, Kornelius Nielsch, Slawomir Prucnal, and Shengqiang Zhou**

B20-type transition-metal silicides or germanides are noncentrosymmetric materials hosting magnetic skyrmions, which are promising information carriers in spintronic devices. The prerequisite is to prepare thin films on technology-relevant substrates with magnetic skyrmions stabilized at a broad temperature and magnetic-field working window. A canonical example is the B20-MnSi film grown on Si substrates. However, the as-yet unavoidable contamination with $MnSi_{1.7}$ occurs due to the lower nucleation temperature of this phase. In this work, a simple and efficient method to overcome this problem and prepare single-phase MnSi films on Si substrates is reported. It is based on the millisecond reaction between metallic Mn and Si using flash-lamp annealing (FLA). By controlling the FLA energy density, single-phase MnSi or $MnSi_{1.7}$ or their mixture can be grown at will. Compared with bulk MnSi, the prepared MnSi films show an increased Curie temperature of up to 41 K. In particular, the magnetic skyrmions are stable over a much wider temperature and magnetic-field range than reported previously. The results constitute a novel phase selection approach for alloys and can help to enhance specific functional properties, such as the stability of magnetic skyrmions.

1. Introduction

Magnetic skyrmions are topologically protected spin configurations[1,2] and have been experimentally discovered in a series of magnetic compounds with noncentrosymmetric crystal structure, such as B20-type transition-metal silicides or germanides.[3–5] In those materials, the Dzyaloshinskii Moriya (DM) interaction and Heisenberg exchange interaction compete with each other, resulting in the formation of a whirling spin structure. The size of skyrmions or the associated magnetic modulation period is determined by the ratio between the magnitudes of the DM interaction and the ferromagnetic exchange interaction, and typically ranges from 1 to 100 nm.[4–8] To drive skyrmions, a much smaller current is needed in comparison to those used to generate spin transfer torques in ferromagnetic metals, which results in lower power consumption and decreases the Joule heat.[9–11] Magnetic skyrmions are proposed for applications in new-generation data storage.[12,13]

B20-type MnSi is regarded as the canonical example, in which magnetic skyrmions were first observed.[3] Up to now, though bulk B20-MnSi compounds are relatively easy to fabricate by rod-casting furnace or Czochralski method,[14,15] skyrmions are only stable in very narrow temperature and magnetic-field ranges.[3] Thin films of B20-MnSi exhibit a much broader temperature range for the existence of skyrmions.[16] Moreover, the preparation of thin film materials on technology-relevant substrates (such as Si) is a prerequisite for today's information technology. B20-type

Z. C. Li, Y. F. Xie, Dr. Y. Yuan, V. Begeza, Dr. L. Cao, Dr. R. Hübner, Dr. L. Rebohle, Prof. M. Helm, Dr. S. Prucnal, Dr. S. Q. Zhou
Helmholtz-Zentrum Dresden-Rossendorf
Institute of Ion Beam Physics and Materials Research
Bautzner Landstrasse 400, D-01328 Dresden, Germany
E-mail: zichao.li@hzdr.de; yuanye@sslab.org.cn; s.zhou@hzdr.de

Z. C. Li, Prof. K. Nielsch
Institute of Materials Science
Technische Universität Dresden
01069 Dresden, Germany

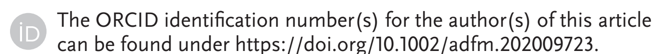
The ORCID identification number(s) for the author(s) of this article can be found under https://doi.org/10.1002/adfm.202009723.

© 2021 The Authors. Advanced Functional Materials published by Wiley-VCH GmbH. This is an open access article under the terms of the Creative Commons Attribution-NonCommercial-NoDerivs License, which permits use and distribution in any medium, provided the original work is properly cited, the use is non-commercial and no modifications or adaptations are made.

DOI: 10.1002/adfm.202009723

Y. F. Xie, V. Begeza, Prof. M. Helm, Prof. K. Nielsch
Institute of Applied Physics
Technische Universität Dresden
01062 Dresden, Germany

Dr. Y. Yuan
Songshan Lake Materials Laboratory
Dongguan, Guangdong 523808, People's Republic of China

Dr. Y. D. Ji
Department of Applied Physics
College of Science
Nanjing University of Aeronautics and Astronautics
Nanjing, Jiangsu 211106, People's Republic of China

Prof. K. Nielsch
Institute for Metallic Materials
IFW-Dresden
01069 Dresden, Germany

MnSi films have been prepared by molecular beam epitaxy and solid-phase epitaxy.[17–20] However, several scientific issues remain challenging for the MnSi thin-film growth. The most important one is the coexistence of the $MnSi_{1.7}$ impurity phase always with MnSi.[19] Another one is that the film can only be grown to a limited thickness of around 30 nm; for larger film thicknesses the stability of skyrmions is deteriorated.[15] From the equilibrium Mn–Si phase diagram, it is found that the B20-MnSi phase is very sensitive to the ratio of the Mn and Si composition.[21] Diffusion induced ingredient fluctuations will result in the formation of $MnSi_{1.7}$. Moreover, $MnSi_{1.7}$ has a lower crystallization temperature than MnSi,[19,22,23] and grows naturally as a parasitic phase in the heating or cooling process during the solid-state reaction. $MnSi_{1.7}$ is a weak itinerant magnet and exhibits excellent thermoelectric properties.[24,25] Recently, it was suggested that $MnSi_{1.7}$ can apply strain to MnSi and increase its Curie temperature.[26] Therefore, separating the MnSi and $MnSi_{1.7}$ phases and/or controlling their mixture ratio is challenging, but is necessary in order to optimize the functionality and to design the topological magnetic properties of MnSi films on demand. This is exactly the question to be tackled in this article.

The relationship between the nucleation activation energy Q, the heating rate Φ, and the crystallization temperature T_p can be expressed by the Kissinger equation[27]

$$\ln\left(\frac{\Phi}{T_p^2}\right) = -\frac{Q}{RT_p} + C \tag{1}$$

where R is the gas constant, and C is a constant ($C = \frac{AR}{Q}$, A is pre-exponential factor also known as the frequency factor). For a particular crystalline phase, when increasing the heating rate Φ, the crystallization temperature will be shifted to higher temperatures. The interval of the crystallization temperatures for different phases will be enlarged. So, different phases can be separated and the microstructure can be selected. Moreover, in the situation of ultrafast heating, the temperature increases so fast that the phase with lower crystallization temperature cannot nucleate within such a short time. This has been demonstrated for CuZr-based metallic glasses in ref. [28]. In particular, by increasing the heating rate above 250 Ks^{-1}, the ductile B2 phase has been selectively formed and the formation of the low-temperature brittle phases $CuZr_2$ and $Cu_{10}Zr_7$ is suppressed. The fast heating and cooling rates make the system-temperature cross the crystallization temperature of brittle phases in a very short time. There is no nucleation time for the brittle phases due to the transient heating and cooling processes. This approach also works well for amorphous Au-based and Pt-based alloys.[29,30] Therefore, we anticipate that a fast annealing method, such as flash-lamp annealing (FLA),[31] provides an effective way to separate B20-MnSi and $MnSi_{1.7}$ and to control the ratio between both phases. During FLA, the sample is exposed to xenon flash lamps, such that the total energy budget is low, leading to a fast heating and cooling rate. The details can be found in the Supporting Information.

In this manuscript, we report the fabrication of phase-controlled $MnSi_x$ films by the solid-state reaction of metallic Mn layers with Si during millisecond flash-lamp annealing. By controlling the energy density deposited to the sample surface by the flash lamps, single-phase B20-MnSi, $MnSi_{1.7}$ or their controlled mixture can be fabricated. The obtained B20-MnSi thin film has a high Curie temperature of 41 K and exhibits characteristic signatures of magnetic skyrmions. The formation window of skyrmions in our film is significantly enlarged with respect to the magnetic field (2–10 kOe) or temperature (up to 41 K) range compared to previously published results.[3,15,17]

2. Results

2.1. MnSi and $MnSi_{1.7}$ Phase Reaction

As shown in **Figure 1**a, depending on different annealing temperatures, two reactions are possible. Due to the ultrafast FLA process, diffusion and nucleation happen at the same time. The diffusion of Si dominates this phase formation process.[32] The reaction at low-temperature is the reaction between Mn and Si, leading to $MnSi_{1.7}$ directly. The reaction at high temperature can form B20-MnSi at the beginning. However, since the Si wafer can provide endless Si atoms, MnSi can further react with extra Si, forming the Si-rich phase, namely $MnSi_{1.7}$. In the conventional solid-state reaction process, $MnSi_{1.7}$ is more easily formed as an inevitable secondary phase in MnSi films. According to our anticipation, a fast or transient reaction between Mn and Si by flash-lamp annealing can inhibit the formation of $MnSi_{1.7}$ by controlling different annealing temperatures with ultrafast heating/cooling rates. In the following, we focus on 3 samples: 4.2R, 4.3R, and 4.3F, which were annealed using flash lamps from the rear-side (R) or from the front-side (F) with the capacitor charged up to 4.2 or 4.3 kV corresponding to the energy density of 134.6 or 139.5 J cm^{-2}, respectively. Therefore, sample 4.2R experienced a lower reaction temperature than sample 4.3R. Sample 4.3F was processed at an intermediate temperature due to the large reflectance of the metallic Mn front side compared to the rough rear side of the Si wafer. In particular, the larger reflectance of the Mn film leads to lower absorbance and therefore lower energy annealing temperature.

Figure 1b displays the XRD patterns obtained from the samples prepared at different annealing parameters. The (111) and (222) diffraction peaks of the Si substrate are at 28.4° and 58.9°, respectively. For sample 4.3R (red, bottom trace) annealed at high temperature, the MnSi-(111) and (222) Bragg peaks are present at 34.2° and 72.4°, respectively. MnSi (210) is also observed at 45° with a much weaker intensity. According to the powder PDF card (01-081-0484),[33] the MnSi (210) peak should be the strongest. Taking into account the intensity ratios between the different diffraction peaks, the majority of the MnSi phase in sample 4.3R is (111)-textured. In comparison to sample 4.3R, sample 4.2R (blue, top trace) shows only the Bragg peaks of $MnSi_{1.7}$. The lower annealing temperature for sample 4.2R promotes the formation of the $MnSi_{1.7}$ single phase. Sample 4.3F (black, middle trace) was processed at an intermediate temperature and shows a mixture of MnSi and $MnSi_{1.7}$. The MnSi phase is also highly (111)-textured. Thus, by tuning the FLA parameters, we have full control over the Mn-silicide phase formation: single-phase B20-MnSi and $MnSi_{1.7}$ are obtained for the highest and lowest annealing temperatures, respectively, which is in accordance with the Kissinger equation.

The in-plane field-dependent magnetizations of these three samples are shown in Figure 1c. Sample 4.3R with single B20-MnSi phase displays multihysteresis, which originates from the transition of different magnetic structures, a typical

© 2021 The Authors. Advanced Functional Materials published by Wiley-VCH GmbH

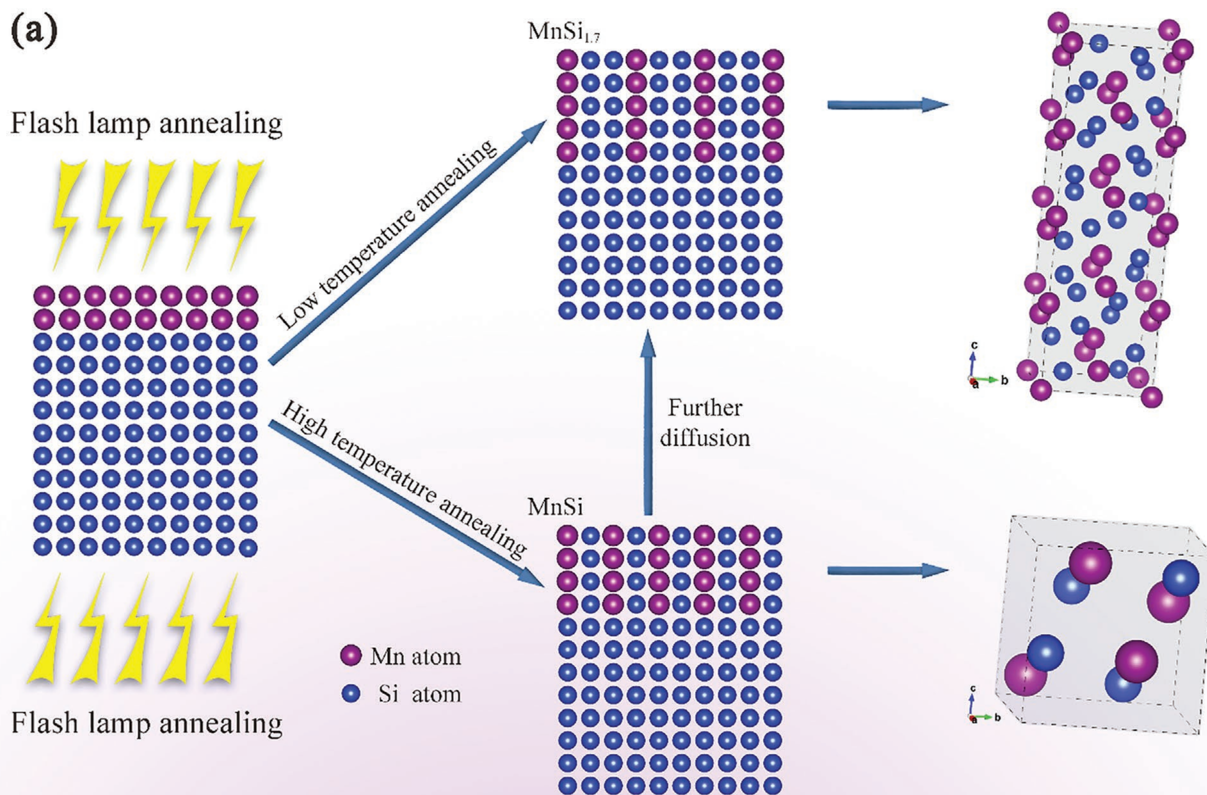

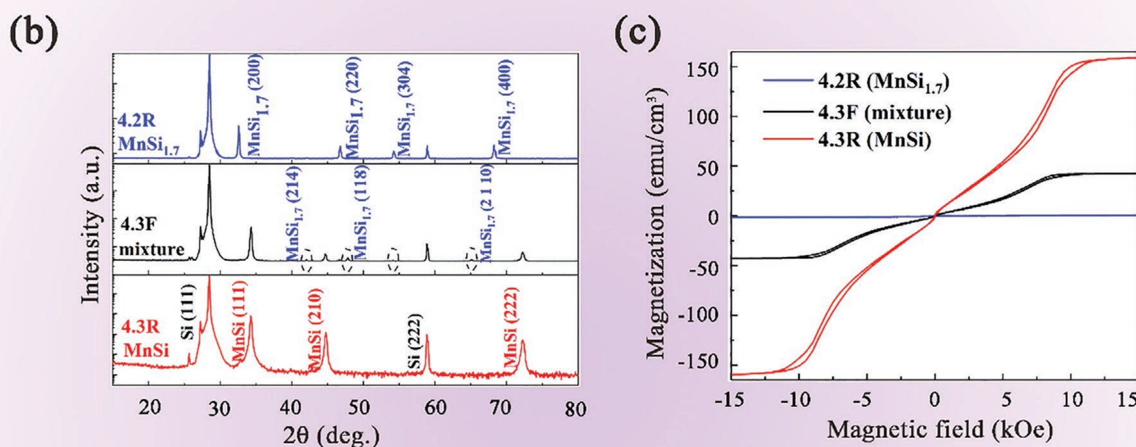

Figure 1. The separation of MnSi and $MnSi_{1.7}$ phases. a) Schematic representation of atom diffusion and solid-state reaction between metal Mn and Si. The blue and purple balls stand for Si and Mn atoms, respectively. $MnSi_{1.7}$ can be formed at low-temperature. B20-MnSi is formed at high temperature. MnSi can further react with Si forming $MnSi_{1.7}$ during cooling down. b) XRD patterns of Mn/Si samples after FLA at different annealing parameters. Single-phase MnSi (bottom, red trace) or $MnSi_{1.7}$ (top, blue trace) was formed in sample 4.3 or 4.2 R, respectively. Sample 4.3F (an enlarged XRD pattern is shown in the Supporting Information) is a mixture of MnSi and $MnSi_{1.7}$. c) In-plane magnetic hysteresis curves recorded at 5 K for the same set of samples. As expected, the magnetization is the highest for the sample containing only B20-type MnSi. The sample containing only $MnSi_{1.7}$ shows negligible magnetization. By the transient reaction between Mn and Si via millisecond flash-lamp annealing, we can synthesize single-phase MnSi or $MnSi_{1.7}$, as well as their mixture at will.

magnetic feature of B20-MnSi.[16,17] The sample 4.3F reveals much reduced magnetization due to the fact that it also contains $MnSi_{1.7}$. As is well known, $MnSi_{1.7}$ is a weak itinerant magnet with a saturation magnetization of 0.012 μB Mn^{-1}.[34] As expected, sample 4.2R containing only $MnSi_{1.7}$ shows negligible magnetization in comparison with the other two samples.

Figure 2a–d shows cross-sectional bright-field transmission electron microscopy (TEM) images a,c) and energy-dispersive X-ray spectroscopy (EDXS)-based element distributions obtained in scanning TEM mode b,d) for the samples 4.2R and 4.3R, respectively. According to Figure 2a,b, sample 4.2R is characterized by a continuous $MnSi_{1.7}$ film with a thickness of around 90 nm and a sharp interface to the Si substrate. Besides an amorphous Mn–Si oxide capping layer and isolated crystalline Si inclusions between this oxide and the $MnSi_{1.7}$ film, there is no other Mn–Si compound. In contrast, for sample

 © 2021 The Authors. Advanced Functional Materials published by Wiley-VCH GmbH

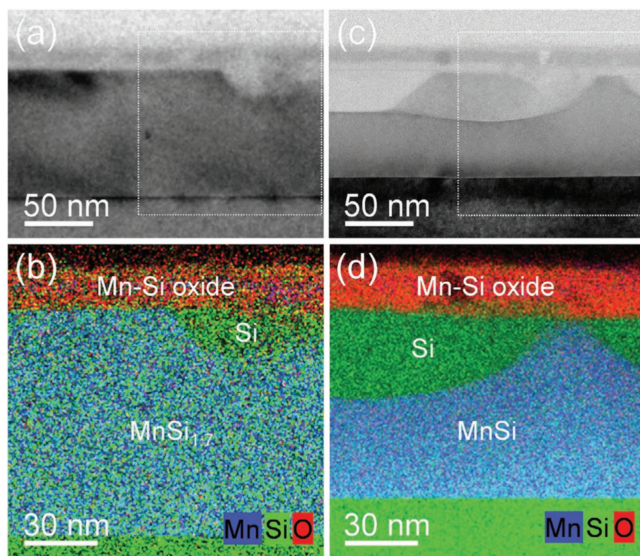

Figure 2. Cross-sectional bright-field TEM images a,c) and EDXS-based element distributions b,d) (Mn: blue, Si: green, O: red) for the samples 4.2 (left) and 4.3R (right) confirming the presence of a continuous single-phase $MnSi_{1.7}$ and MnSi film, respectively, each characterized by a sharp interface to the Si substrate. Thus $MnSi_{1.7}$ and MnSi thin films can be synthesized at will by controlling the flash energy density.

4.3R, an up to 75 nm thick continuous single-phase B20-type MnSi film is obtained (Figure 2c,d). Moreover, extra Si from the substrate can diffuse through the MnSi layer, and an amorphous Mn–Si oxide capping layer protects the sample from further oxidation. The TEM analyses, which are described in more detail in Figures S5 and S6 (Supporting Information), well corroborate the XRD and magnetization measurements. By controlling the reaction temperature during millisecond flash-lamp annealing, we can obtain films of pure tetragonal $MnSi_{1.7}$, of pure cubic B20-type MnSi or of their mixture.

2.2. Magnetic Skyrmions

Lorentz transmission electron microscopy (LTEM), magnetic force microscopy and neutron scattering can give direct confirmation of magnetic skyrmions in real or reciprocal space.[3,4,7,15,16,26,35] For MnSi thin films, both LTEM and magnetization measurements were performed on the same sample and provided consistent results.[16] Therefore, magnetization and magneto-transport measurements are also accepted as methods to characterize magnetic skyrmions.[16,17,36] In this section, we present a detailed magnetic and electrical investigation of sample 4.3R, which contains only the B20-MnSi phase. The MnSi film prepared by our method exhibits nontrivial magnetic properties as known from samples prepared by other methods.[15,16,37]

Figure 3a shows the temperature-dependent saturation magnetization for the B20-MnSi film. The derivative dM/dT of the

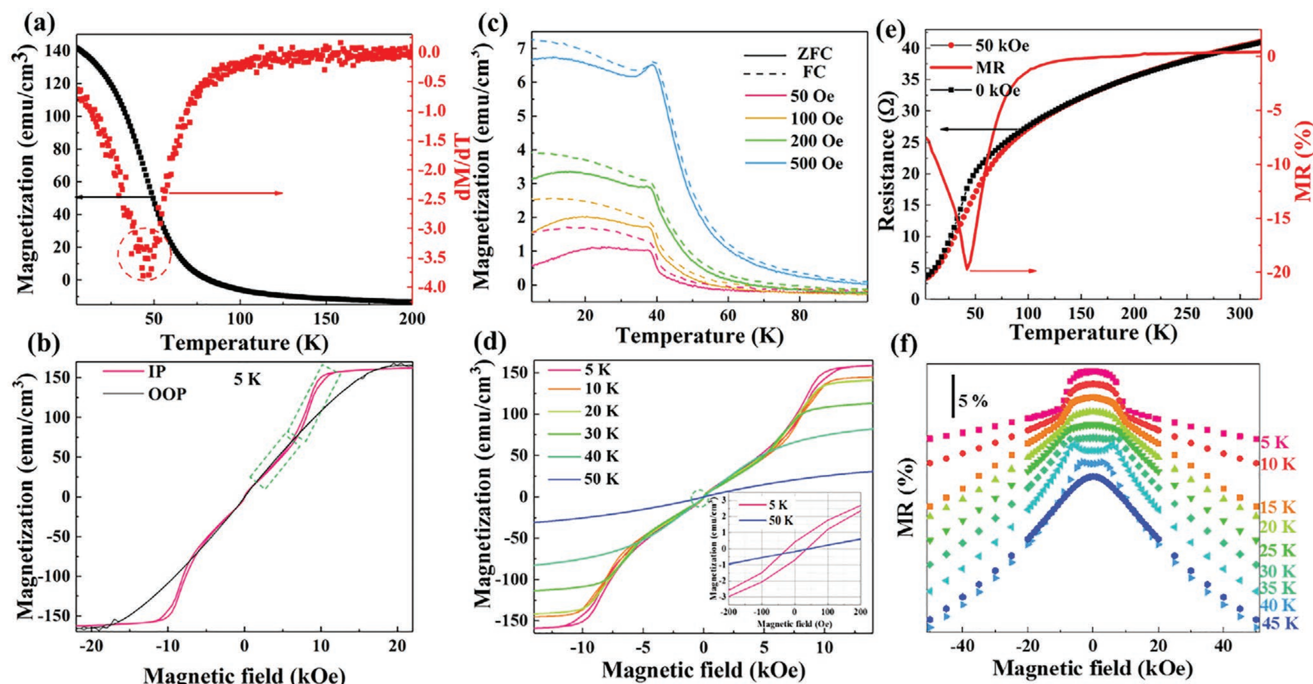

Figure 3. a) In-plane saturation magnetization and the calculated dM/dT. The valley of dM/dT at around 41 K indicates the Curie temperature or the transition from ferromagnetic to paramagnetic. b) In-plane and out-of-plane MH curves recorded at 5 K. The easy axis and multihysteresis are stabilized in-plane. The areas of green dotted rectangles show multihysteresis. c) In-plane field cooling (FC) and zero field cooling (ZFC) magnetization measured under different magnetic fields. There is also a kink around 41 K, which is the transition from helical to paramagnetic. d) In-plane MH curves measured at different temperatures. The inset shows the data around the origin. e) Temperature-dependent resistance under 0 (black square) and 50 kOe (red circle) fields. The red solid line is the calculated MR at 50 kOe. f) Magnetic field-dependent magnetoresistance at various temperatures. The anomalous behaviour disappears at 45 K (above the Curie temperature).

© 2021 The Authors. Advanced Functional Materials published by Wiley-VCH GmbH

MT curve has a minimum at 41 K, indicating the Curie temperature, which is higher than for bulk MnSi (29.5 K[3]) due to the tensile strain in the MnSi film[16,19,38] (see also the Raman analysis in Section 4 in the Supporting Information[39,40]). The ZFC/FC magnetization under different magnetic fields is shown in Figure 3c. Near 41 K, a cusp feature is observed. It is the transition from the ground helimagnetic to paramagnetic state above 41 K. When increasing the magnetic field, the cusp becomes more pronounced. The shift and disappearance of this cusp are shown in the Supporting Information, which prove the transformations of different magnetic structures again.

Magnetic hysteresis loops at 5 K of the up to 75 nm thick MnSi film with in-plane and out-of-plane magnetic fields reveal the in-plane easy axis favored by the shape anisotropy,[19,41] as shown in Figure 3b. Moreover, both hysteresis loops show almost zero remanence, indicating the formation of a multidomain state at zero field. The saturation field is about 13 and 19 kOe for the in-plane and out-of-plane direction, respectively. In addition, the multihysteresis feature is observed only in-plane, indicating Bloch-type skyrmions.[42] Figure 3d shows in-plane MH curves at various temperatures, where the MH curves have multihysteresis below the Curie temperature. This suggests the transformation between different spin structures. For better visualization, enlarged MH curves from −200 to 200 Oe are shown in the inset of Figure 3d. Magnetic hysteresis disappears above the Curie temperature, where the material becomes paramagnetic.

The electrical resistances of the MnSi film under a magnetic field of 0 and 50 kOe are shown as a function of temperature in Figure 3e. The resistance increases with increasing temperature, which means that the MnSi film behaves like a metal.[43] The calculated magnetoresistance (MR), $MR = \frac{R_H - R_0}{R_0} \times 100\%$ (R_H: resistance at 50 kOe, R_0: resistance at zero field), is shown as a red solid line in Figure 3e. The negative magnetoresistance in MnSi can be understood as follows: the magnetic field increases the effective field acting on the localized spins and suppresses the fluctuation of spins in space and time, which leads to a decrease of the resistivity.[43] The peak of (negative) MR at around 41 K implies that the largest resistance change occurs near the Curie temperature.

The magnetoresistance of the MnSi film at various temperatures is shown in Figure 3f. Below the Curie temperature, it shows an anomalous phenomenon at low magnetic field. More MR data around the Curie temperature is presented in the Supporting Information. Above the Curie temperature, the MR becomes normal without any specific features, which is consistent with bulk MnSi.[43]

In **Figure 4**a,c, the derivatives of the static magnetization dM/dH show four critical transition fields, termed as H_β, $H_{\alpha1}$, $H_{\alpha2}$, and H_{sat}. The dashed lines show their shift depending on temperature. H_{sat} is the critical field, above which the material changes into field-polarized ferromagnetism. Below H_β, the system is at its ground helicoid state. At 40 K, there is no clear

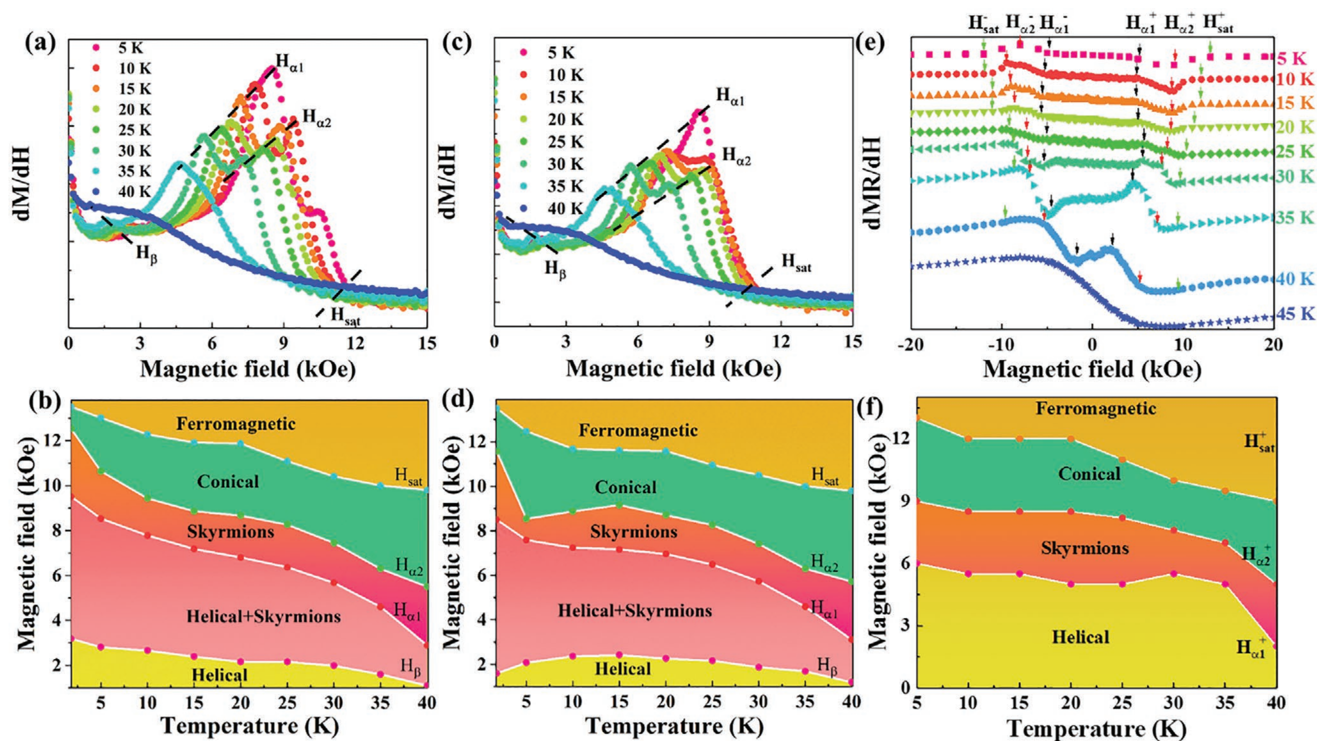

Figure 4. Static susceptibility in increasing a) and decreasing c) field sweeps for the MnSi film at various temperatures. Black dashed lines in (a) and (c) show the shift of transition fields at each temperature. Four critical fields are identified and labeled as H_β, $H_{\alpha1}$, $H_{\alpha2}$, and H_{sat}. $H_{\alpha1}$ and $H_{\alpha2}$ bound the region of stable elliptic skyrmions. The dashed lines define the boundary for metastable helicoids H_β and ferromagnetic H_{sat}. Magnetic phase diagram in increasing b) and decreasing d) field. With increasing temperature, these magnetic phases (Helical, Helical + Skyrmions, Skyrmions, Conical, and Ferromagnetic) can be formed at lower fields. e) Calculated dMR/dH from data in Figure 3 . The black, red, and green arrows stand the position of $H_{\alpha1}$, $H_{\alpha2}$, and H_{sat}, respectively. f) Magnetic phase diagram of the MnSi film with respect to temperatures and magnetic fields.

© 2021 The Authors. Advanced Functional Materials published by Wiley-VCH GmbH

peak resolvable, but only a plateau, meaning the smearing out of phase boundary near the Curie temperature. With decreasing temperature, we observe two apparent peaks at $H_{\alpha 1}$ and $H_{\alpha 2}$, indicating the appearance of another phase. The first-order transitions in and out of this phase bounded by $H_{\alpha 1}$ and $H_{\alpha 2}$ indicate a difference in topology between this state and the neighbouring ferromagnetic (above $H_{\alpha 2}$) and helicoid (below $H_{\alpha 1}$) states. The phase between $H_{\alpha 1}$ and $H_{\alpha 2}$ is the so-called skyrmion phase.[15,16] Above $H_{\alpha 2}$, the skyrmion phase nearly vanishes and the system evolves via a first-order phase transition into a conical state. With increasing field from H_{β} to $H_{\alpha 1}$, the system changes into a metastable helicoid state. Compared with field-increase and decrease processes, these transition fields show a small difference below 15 K due to the hysteresis. However, above 15 K these transition fields do not change significantly with respect to field increase or decrease due to the coinciding of MH curves.

The temperature-dependent transition fields are plotted in Figure 4b,d. With increasing the magnetic field, the magnetic structure transforms into the Helical, Helical + Skyrmions, Skyrmions, Conical, and Ferromagnetic phase. Compared with other B20-MnSi, skyrmions in our MnSi film can be stabilized over the whole temperature range below the Curie temperature and a wider magnetic field range of around 10 kOe.[15,16] It is known that the temperature and magnetic field intervals of skyrmions become narrower with increasing the thickness of the MnSi film.[4,15] However, our MnSi film has a thickness of up to 75 nm and is thicker than other reported MnSi films.[17] This enlarged skyrmion stability in wider temperature and magnetic field ranges offers more flexibility in spintronic applications.[9,10,44] It is speculated that the reaction by flash-lamp annealing stabilizes the strain above the critical thickness, therefore increasing both the Curie temperature and the stability of skyrmions.

Indeed, by analyzing the magnetoresistance one also can investigate the field-driven evolution of the spin textures in MnSi.[41,45] As shown in Figure 4e, we examine more closely the derivative dMR/dH for the same data displayed in Figure 3f. We defined the transition fields $H_{\alpha 1}$, $H_{\alpha 2}$, and H_{sat}, as marked by the arrows. Values for positive and negative magnetic fields are denoted by the superscripts "+" and "–", respectively. However, the transition from Helical to Helical + Skyrmions is not resolved probably due to the negligible MR variation, being consistent with previous reports.[5,41,45] With increasing magnetic field, the helimagnetic phase transforms into skyrmions via a first order phase transition, manifested as peaks at $H_{\alpha 1}$ due to the completely different topological properties between helimagnetic and skyrmions. Above the critical field $H_{\alpha 2}$, the system transforms into the conical phase. Skyrmions can be stabilized at the range between $H_{\alpha 1}$ and $H_{\alpha 2}$. H_{sat} is the critical magnetic field, above which MnSi changes into the ferromagnetic state. Figure 4f shows the magnetic phase diagram of MnSi. Compared with Figure 4b,d, this magnetic phase diagram obtained from MR shows qualitatively the same temperature and magnetic-field range for skyrmions.

2.3. Discussion and Outlook

There are 4 stable Mn–Si compounds. With increasing Si concentration, Mn_3Si, Mn_5Si_3, B20-MnSi, and higher manganese silicides can form at thermal equilibrium. Characterized by tetragonal crystal structures with different *c*-axis lengths, higher manganese silicides have many chemical formulas such as: Mn_4Si_7, $Mn_{11}Si_{19}$, $Mn_{15}Si_{26}$, and $Mn_{27}Si_{47}$ and are generally written as $MnSi_{1.7}$.[34,46] The single B20-MnSi phase can only form at 50 at% Si and $MnSi_{1.7}$ exists from 55 to 95 at% Si. In a Mn–Si thin film grown on Si substrates, the richness of Si makes the Mn_3Si and Mn_5Si_3 phase hard to form due to the limited amount of Mn. However, $MnSi_{1.7}$ is much easier to form in these thin films. Moreover, the crystallization temperature for B20-MnSi is 1276 °C, which is higher than 1150 °C for $MnSi_{1.7}$. This means that $MnSi_{1.7}$ can nucleate prior to B20-MnSi in thermal equilibrium condition. Therefore, $MnSi_{1.7}$ often coexists with B20-MnSi in thin films grown by solid-phase epitaxy.[19] The equilibrium phase diagram of the Mn–Si system is shown in Figure S2a in the Supporting Information.

During flash-lamp annealing, the heating and cooling rates are much higher compared to conventional rapid thermal annealing and can be adjusted by controlling the energy budget, i.e., the flash energy density delivered to the sample surface. However, we cannot measure the temperature in situ. Presumably, by increasing the heating rate above a threshold (see Figure S2b, Supporting Information), the high-temperature phase can be selectively formed and the formation of low-temperature phases will be suppressed, as schematically shown in Figure S2b (Supporting Information). Therefore, this fast annealing method leads to a transient reaction between Mn and Si, serving as an effective way to separate B20-MnSi and $MnSi_{1.7}$ and to control the ratio between MnSi and $MnSi_{1.7}$ in the presence of both phases. Note that for this purpose the fast reaction and the high heating/cooling rate are important. This approach is not only limited to flash lamps. Millisecond lasers are expected to lead to similar effects and have been widely used in semiconductor industry.[47]

Both magnetron sputtering and flash-lamp annealing are ready to be scaled up to whole Si wafers. Therefore, this approach can be integrated with the existing and well-developed Si microelectronic technology. As shown in Figure 2a, our $MnSi_{1.7}$ film has a reasonable flat interface and surface. The surface oxide can be selectively etched by acids (e.g., HF). By applying lithography to pattern the Mn film and therefore the $MnSi_{1.7}$ film, one can integrate a stand-along, thermoelectric power source to Si-based devices on a single chip.[48] The top surface of B20-MnSi layer is still not smooth enough. This might be due to the slight oxidation of the Mn metal film right before annealing. However, the surface can be processed by well-developed chemical-mechanical planarization.[49] Nevertheless, the much higher Curie temperature and the broader magnetic-field and temperature window for stabilizing skyrmions in our MnSi film are profound advantages. They might be exclusively related with the ultrafast thermal processing.

3. Conclusion

In summary, by controlling the reaction parameters using strongly nonequilibrium flash-lamp annealing, we have full control over the phase formation of Mn–silicides in thin films from single-phase B20-MnSi or $MnSi_{1.7}$ to mixed phases. The

© 2021 The Authors. Advanced Functional Materials published by Wiley-VCH GmbH

obtained films are highly textured and reveal sharp interfaces to the Si substrate. The obtained B20-MnSi films exhibit a high Curie temperature at 41 K. The skyrmion phase can be stabilized in broad temperature and magnetic-field ranges. We propose millisecond intense pulse light annealing as a general approach for phase separation in transition-metal silicides and germanides and for the growth of B20-type films with enhanced topological stability.

4. Experimental Section

Sample Preparation: In order to fabricate the MnSi films, a 30 nm thick Mn film was first deposited on a Si (111) wafer by DC magnetron sputtering. Afterward, FLA was employed to anneal the samples at different annealing parameters, rendering the reaction between Mn and Si. The FLA device is made by Rovak GmbH, and illustrated in Figure S1 (Supporting Information). During annealing, the samples were heated up by 12 Xe 30 cm long lamps in a continuous N_2 flow.[31] The annealing temperature was controlled by varying the power density. 4.2R, 4.3R, and 4.3F represent the samples with annealing parameters of 4.2 kV (Voltage applied to the capacitor of the flash lamps, to produce an intense flash pulse) from the rear side (4.2R), 4.3 kV from the rear side (4.3R) and 4.3 kV from the front side (4.3F), respectively. For all samples, the flash duration was 20 ms. 4.2 or 4.3 kV is the high voltage to charge the flash lamps, which corresponds to an energy density of 134.6 and 139.5 J cm^{-2}. Generally, a higher voltage generates a higher temperature on the surface if the absorbance of the materials are the same. The annealing from the front side (4.3F) is supposed to generate a slightly lower temperature than 4.3R due to the large reflectivity of the Mn metal film than the Si wafer. With a 20 ms pulse duration, the heating and cooling rates are estimated to be 80 000 and 160 Ks^{-1}, respectively. When the sample was annealed by flash-lamp from the rear side, the Si wafer absorbed the light and was heated-up to high temperature, then transferred the energy to the Mn layer. At high temperature, Si atoms diffused into the Mn layer. After the reaction between Mn and Si, extra Si can further diffuse to the sample surface and form crystalline Si (see Figure 2). Its formation can be minimized or eliminated by further optimizing the Mn thickness and the annealing parameters. Being different from ref. [28], in which the electrical current was used to induce heating in bulk materials and the heating rate was in the range of 250–700 Ks^{-1}, a light pulse was used. The approach is better suitable for thin-film materials and can reach much higher heating rates, which are crucial for the phase selection of synthesized silicides and germanides.

Structure Characterization: X-ray diffraction (XRD) and transmission electron microscopy (TEM) were employed to analyze the microstructure of the obtained films. XRD was performed at room temperature on a Bruker D8 Advance diffractometer with a Cu-target source. The measurements were done in Bragg–Brentano-geometry with a graphite secondary monochromator and a scintillator detector. Bright-field and high-resolution TEM imaging were performed on an image-C_s-corrected Titan 80–300 microscope (FEI) operated at an accelerating voltage of 300 kV. High-angle annular dark-field scanning transmission electron microscopy (HAADF-STEM) imaging and spectrum imaging analysis based on energy-dispersive X-ray spectroscopy (EDXS) were done at 200 kV with a Talos F200X microscope equipped with an X-FEG electron source and a Super-X detector system (FEI).

Magnetic and Transport Property Measurements: The magnetization of the films was measured by a superconducting quantum interference device equipped with a vibrating sample magnetometer (SQUID-VSM) with the field parallel (in-plane) or perpendicular (out-of-plane) to the films. For the zero field cooling (ZFC) measurements, the samples were cooled down to 5 K under a zero field, then different fields were applied and magnetization data were collected during the warming-up process. When reaching 100 K, the samples were recooled to 5 K at the same field while the data recording was continued. This process was called field cooling (FC). The transport properties of the MnSi film were investigated by a Lake Shore Hall measurement system. Magnetic-field dependent resistance was measured between 5 and 300 K using the van der Pauw geometry. In the resistivity measurement the magnetic field was applied along the sample surface plane (in-plane).

Supporting Information

Supporting Information is available from the Wiley Online Library or from the author.

Acknowledgements

The authors acknowledge R. Aniol for TEM specimen preparation, A. Scholz for XRD measurements and R. Uhlemann for the technical support. The authors are grateful to U. K. Rößler for some discussions. The author Z. Li and Y. Xie acknowledge the financial support by China Scholarship Council (File No. 201707040077 and 201706340054, respectively). The use of the HZDR Ion Beam Center TEM facilities and the funding of TEM Talos by the German Federal Ministry of Education of Research (BMBF), Grant No. 03SF0451, in the framework of HEMCP are acknowledged. S.Z. thanks financial support from the German Research Foundation (ZH 225/6-1).

Open access funding enabled and organized by Projekt DEAL.

Conflict of Interest

The authors declare no conflict of interest.

Data Availability Statement

Research data are not shared.

Keywords

B20-MnSi, flash-lamp annealing, phase separation, skyrmions

Received: November 13, 2020
Revised: January 8, 2021
Published online: February 8, 2021

[1] A. N. Bogdanov, D. A. Yablonskii, *Sov. Phys. JETP* **1989**, *68*, 101.
[2] U. K. Rößler, A. N. Bogdanov, C. Pfleiderer, *Nature* **2006**, *442*, 797.
[3] S. Mühlbauer, B. Binz, F. Jonietz, C. Pfleiderer, A. Rosch, A. Neubauer, R. Georgii, P. Böni, *Science* **2009**, *323*, 915.
[4] X. Z. Yu, Y. Onose, N. Kanazawa, J. H. Park, J. H. Han, Y. Matsui, N. Nagaosa, Y. Tokura, *Nat. Mater.* **2011**, *10*, 106.
[5] M. J. Stolt, S. Schneider, N. Mathur, M. J. Shearer, B. Rellinghaus, K. Nielsch, S. Jin, *Adv. Funct. Mater.* **2019**, *29*, 1805418.
[6] M. Yang, Q. Li, R. V. Chopdekar, R. Dhall, J. Turner, J. D. Carlström, C. Ophus, C. Klewe, P. Shafer, A. T. N'Diaye, J. W. Choi, G. Chen, Y. Z. Wu, C. Hwang, F. Wang, Z. Q. Qiu, *Sci. Adv.* **2020**, *6*, eabb5157.
[7] M. Raju, A. Yagil, A. Soumyanarayanan, A. K. Tan, A. Almoalem, F. Ma, O. Auslaender, C. Panagopoulos, *Nat. Commun.* **2019**, *10*, 696.

© 2021 The Authors. Advanced Functional Materials published by Wiley-VCH GmbH

[8] W. Legrand, D. Maccariello, N. Reyren, K. Garcia, C. Moutafis, C. Moreau-Luchaire, S. Collin, K. Bouzehouane, V. Cros, A. Fert, *Nano Lett.* **2017**, *17*, 2703.
[9] F. Jonietz, S. Mühlbauer, C. Pfleiderer, A. Neubauer, W. Münzer, A. Bauer, T. Adams, R. Georgii, P. Böni, R. A. Duine, K. Everschor, M. Garst, A. Rosch, *Science* **2010**, *330*, 1648.
[10] A. Fert, V. Cros, J. Sampaio, *Nat. Nanotechnol.* **2013**, *8*, 152.
[11] Y. Luo, S. Z. Lin, M. Leroux, N. Wakeham, D. M. Fobes, E. D. Bauer, J. B. Betts, J. D. Thompson, A. Migliori, B. Maiorov, *Commun. Mater.* **2020**, *1*, 83.
[12] D. Maccariello, W. Legrand, N. Reyren, K. Garcia, K. Bouzehouane, S. Collin, V. Cros, A. Fert, *Nat. Nanotechol.* **2018**, *13*, 233.
[13] E. Ruff, S. Widmann, P. Lunkenheimer, V. Tsurkan, S. Bordács, I. Kézsmárki, A. Loidl, *Sci. Adv.* **2015**, *1*, e1500916.
[14] A. Neubauer, C. Pfleiderer, B. Binz, A. Rosch, R. Ritz, P. G. Niklowitz, P. Böni, *Phys. Rev. Lett.* **2009**, *102*, 186602.
[15] X. Yu, A. Kikkawa, D. Morikawa, K. Shibata, Y. Tokunaga, Y. Taguchi, Y. Tokura, *Phys. Rev. B* **2015**, *91*, 054411.
[16] Y. Li, N. Kanazawa, X. Z. Yu, A. Tsukazaki, M. Kawasaki, M. Ichikawa, X. F. Jin, F. Kagawa, Y. Tokura, *Phys. Rev. Lett.* **2013**, *110*, 117202.
[17] M. N. Wilson, E. A. Karhu, A. S. Quigley, U. K. Rößler, A. B. Butenko, A. N. Bogdanov, M. D. Robertson, T. L. Monchesky, *Phys. Rev. B* **2012**, *86*, 144420.
[18] E. A. Karhu, S. Kahwaji, M. D. Robertson, H. Fritzsche, B. J. Kirby, C. F. Majkrzak, T. L. Monchesky, *Phys. Rev. B* **2011**, *84*, 060404(R).
[19] E. A. Karhu, S. Kahwaji, T. L. Monchesky, C. Parsons, M. D. Robertson, C. Maunders, *Phys. Rev. B* **2010**, *82*, 184417.
[20] S. Higashi, Y. Ikedo, P. Kocan, H. Tochihara, *Appl. Phys. Lett.* **2008**, *93*, 013104.
[21] P. Villars, *Springer Science Materials*, Springer, Heidelberg **2016**.
[22] S. Tang, I. Kravchenko, J. Yi, G. Cao, J. Howe, D. Mandrus, N. Materials, O. Ridge, *Nano Res.* **2014**, *7*, 1788.
[23] N. L. Okamoto, T. Koyama, K. Kishida, K. Tanaka, H. Inui, *Acta Mater.* **2009**, *57*, 5036.
[24] Z. Li, J. F. Dong, F. H. Sun, Asfandiyar, Y. Pan, S. F. Wang, Q. Wang, D. Zhang, L. Zhao, J. F. Li, *Adv. Sci.* **2018**, *5*, 1800626.
[25] G. Kim, H. Kim, H. Lee, J. Kim, K. Lee, J. W. Roh, W. Lee, *Nano Energy* **2020**, *72*, 104698.
[26] A. S. Sukhanov, P. Vir, A. Heinemann, S. E. Nikitin, D. Kriegner, H. Borrmann, C. Shekhar, C. Felser, D. S. Inosov, *Phys. Rev. B* **2019**, *100*, 180403(R).
[27] H. E. Kissinger, *Anal. Chem.* **1957**, *29*, 1702.
[28] I. V. Okulov, I. V. Soldatov, M. F. Sarmanova, I. Kaban, T. Gemming, K. Edström, J. Eckert, *Nat. Commun.* **2015**, *6*, 7932.
[29] X. Monnier, D. Cangialosi, B. Ruta, R. Busch, S. Gallino, *Sci. Adv.* **2020**, *6*, eaay1454.
[30] S. Sohn, Y. Xie, Y. Jung, J. Schroers, J. J. Cha, *Nat. Commun.* **2017**, *8*, 1980.
[31] L. Rebohle, S. Prucnal, W. Skorupa, *Semicond. Sci. Technol.* **2016**, *31*, 103001.
[32] L. Zhang, D. G. Ivey, *J. Mater. Res.* **1991**, *6*, 1518.
[33] M. Salvo, F. Smeacetto, F. D'Isanto, G. Viola, P. Demitri, F. Gucci, M. J. Reece, *J. Eur. Ceram. Soc.* **2019**, *39*, 66.
[34] U. Gottlieb, A. Sulpice, B. Lambert-Andron, O. Laborde, *J. Alloys Compd.* **2003**, *361*, 13.
[35] Z. Hou, W. Ren, B. Ding, G. Xu, Y. Wang, B. Yang, Q. Zhang, Y. Zhang, E. Liu, F. Xu, W. Wang, G. Wu, X. Zhang, B. Shen, Z. Zhang, *Adv. Mater.* **2017**, *29*, 1701144.
[36] S. X. Huang, C. L. Chien, *Phys. Rev. Lett.* **2012**, *108*, 267201.
[37] N. Kanazawa, S. Seki, Y. Tokura, *Adv. Mater.* **2017**, *29*, 1603227.
[38] A. I. Figueroa, S. L. Zhang, A. A. Baker, R. Chalasani, A. Kohn, S. C. Speller, D. Gianolio, C. Pfleiderer, G. van der Laan, T. Hesjedal, *Phys. Rev. B* **2016**, *94*, 174107.
[39] H. M. Eiter, P. Jaschke, R. Hackl, A. Bauer, M. Gangl, C. Pfleiderer, *Phys. Rev. B* **2014**, *90*, 024411.
[40] T. Tite, G. J. Shu, F. C. Chou, Y. M. Chang, *Appl. Phys. Lett.* **2010**, *97*, 031909.
[41] H. F. Du, J. P. DeGrave, F. Xue, D. Liang, W. Ning, J. Y. Yang, M. L. Tian, Y. H. Zhang, S. Jin, *Nano Lett.* **2014**, *14*, 2026.
[42] D. Okuyama, M. Bleuel, J. S. White, Q. Ye, J. Krzywon, G. Nagy, Z. Q. Im, I. Živkovi´c, M. Bartkowiak, H. M. Rønnow, S. Hoshino, J. Iwasaki, N. Nagaosa, A. Kikkawa, Y. Taguchi, Y. Tokura, D. Higashi, J. D. Reim, Y. Nambu, T. J. Sato, *Commun. Phys.* **2019**, *2*, 79.
[43] K. Kadowaki, K. Okuda, M. Date, *J. Phys. Soc. Jpn.* **1982**, *51*, 2433 .
[44] A. Fert, N. Reyren, V. Cros, *Nat. Rev. Mater.* **2017**, *2*, 17031.
[45] H. Du, D. Liang, C. Jin, L. Kong, M. J. Stolt, W. Ning, J. Yang, Y. Xing, J. Wang, R. Che, J. Zang, S. Jin, Y. Zhang, M. Tian, *Nat. Commun.* **2015**, *6*, 7637.
[46] S. Zhou, K. Potzger, G. Zhang, A. Mücklich, F. Eichhorn, N. Schell, R. Grotzschel, B. Schmidt, W. Skorupa, M. Helm, J. Fassbender, *Phys. Rev. B* **2007**, *75*, 0852032007.
[47] O. Gluschenkov, H. Jagannathan, *ECS Trans.* **2018**, *85*, 11.
[48] T. Taniguchi, T. Ishibe, N. Naruse, Y. Mera, Md. M. Alam, K. Sawano, Y. Nakamura, *ACS Appl. Mater. Interfaces* **2020**, *12*, 25428.
[49] P. Zantye, A. Kumar, A. Sikder, *Mater. Sci. Eng. R* **2004**, *45*, 89.

© 2021 The Authors. Advanced Functional Materials published by Wiley-VCH GmbH